Exploration of convolutional neural networks to handle non-linearity estimation issues in pyramid wavefront sensors.

Camilo Weinberger, Felipe Guzmán, Jorge Tapia, Benoît Neichel, Esteban Vera

Exploration of Convolutional Neural Networks to handle non-linearity estimation issues in pyramid wavefront sensors

Camilo Weinberger[a], Felipe Guzmán[a], Jorge Tapia[a], Benoit Neichel[b], and Esteban Vera[a]

[a]School of Electrical Engineering, Pontificia Universidad Católica de Valparaiso, Valparaiso, Chile
[b]Laboratoire d'Astrophysique de Marseille, Marseille, France

ABSTRACT

In this work, we evaluate a especially crafted deep convolutional neural network to provide with estimations of the wavefront aberration modes directly from pyramidal wavefront sensor (PyWFS) images. Overall, the use of deep neural networks allow to improve the estimation performance as well as the operational range of the PyWFS, especially when considering cases of strong turbulence or bad seeing ratios D_0/r_0. Our preliminary results provide with evidence that by using neural nets, instead of the classic linear estimation methods, we can obtain a low modulation sensitivity response while extending the linearity range of the PyWFS, reducing the residual variance by a factor of 1.6 when dealing with a r_0 as low as a few centimeters.

Keywords: Adaptive Optics, Pyramidal Wavefront Sensor, Linearity, Deep Learning, Machine Learning

1. INTRODUCTION

For demanding Adaptive Optics (AO) applications, such as for large telescopes, and soon by extremely large telescopes, the pyramidal wavefront sensor (PyWFS)[1] has demonstrated to deliver the required sensitivity in terms of wavefront measurements. To do so, the PyWFS performs uses a multi-faceted prism, generating multiple sub-pupil versions that are projected onto an imaging detector.

Nevertheless, the PyWFS provides with a trade-off between high sensitivity and low linearity. Fig. 1 illustrates the sensor frame obtained by the same phase map with different strengths. As the strength increases, we can observe that the intensity gets concentrated in fewer pixels, which lead to linearity problems in the estimation.

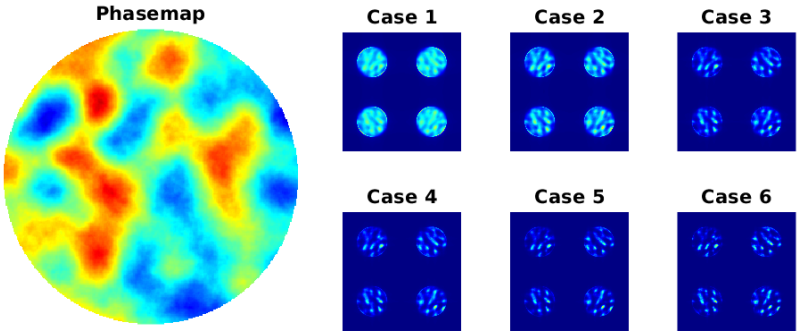

Figure 1: The phase map correspond to a random distribution with a standard deviation of $0.201nm$. Cases 1-6 correspond to the PyWFS image using different multipliers on the input phase map: $2\times$, $4\times$, $5\times$, $7\times$, and $9\times$, respectively.

Moreover, it is relevant to consider that the PyWFS requires a precise alignment of the PSF on top of the apex of the pyramid to deliver a proper estimation of the modes, that would otherwise be dominated by tip and tilt.

Corresponding author information:
Esteban Vera. E-mail: esteban.vera@pucv.cl

To improve this feature, a tip-tilt mirror is used to modulate the PSF around the apex, improving the linearity but diminishing the sensitivity.[2,3] The magnitude of the modulation radius, or simply modulation, is defined as $M = n\lambda/D$, where λ is the wavelength of the light beam, D is the diameter of the spot,[4,5] respectively. When using traditional least-squares estimation methods, an optical gain correction using convolution techniques[6] or external sensors can alleviate the linearity problem.

Without modulation, the linear response solely depend on the spatial correlation r_0 in the pupil. This correlation allows computing a non-dimensional ratio D_0/r_0 where D_0 is the telescope diameter size. This ratio indicates the strength of the turbulence independent of the telescope size.

To solve the non-linearity problems present in the PyWFS, we propose to use the WFNet,[7] a deep neural network especially crafted for deep learning wavefront sensing from intensity images.[8] This convolutional neural network (CNN) can recognize and estimate a specific number of Zernike or K-L modes from a single image taken from a PyWFS. Thus, we aim to improve the linearity response of the PyWFSs in future AO systems when dealing with highly varying turbulence conditions. Fig 2 displays the generative model up to the WFNET which will be responsible of estimating the incoming phase modes.

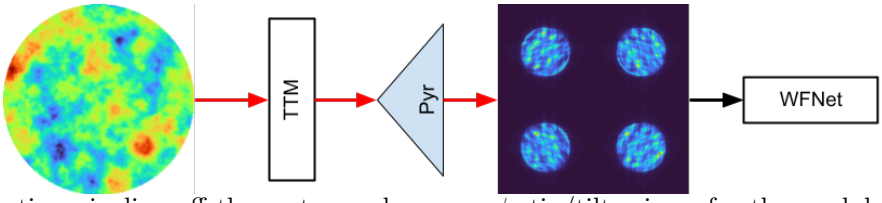

Figure 2: Propagation pipeline off the system: phasemap ϕ, tip/tilt mirror for the modulation, the pyramid glass, and the sensor image, which will feed the WFNET training and estimation processes.

2. SIMULATION

We use the OOMAO[9] toolbox for MATLAB, generating a dataset to train and validate the the performance of the WFNET. OOMAO allows to simulate the optical path of a theoretical telescope up to the WFS detector (Guide Star → Atmosphere → Telescope → Sensor). In this work, the simulation conditions were:

- Natural Guide star: Photometry V. For wavelength of 0.55 microns.
- Atmosphere: A single layer of size 90 km. Seeing ratio D_0/r_0 ranging from 1.6 to 300 respect to the telescope diameter.
- Telescope: $D_0 = 1.5$ m of diameter, Inclination: on Zenith, Resolution of 268 pixels.
- Sensor: 4 faces pyramidal wavefront sensor, modulation $M = 3\lambda/D$.

Regarding data processing, the datasets were standardized using global normalization,[10] and the normalized reference image $\mathrm{I_{Ref}}$ is subtracted. This mathematical operation on the images makes them independent of the star magnitude. The reference image, $\mathrm{I_{Ref}}$, is acquired by propagating a flat phasemap through the simulated optical system. Equation (1) represents the data processing, with I_{Dataset} corresponding to any image from the dataset, $I_{NRaw}(\phi_M)$ corresponds to its normalized version, while $I_N(\phi = 0)$ corresponds to the normalized reference image.

$$I_{Dataset} = I_{NRaw}(\phi_M) - I_N(\phi = 0) \tag{1}$$

We simulate $2 \cdot 10^5$ training samples and $6 \cdot 10^3$ validation samples ranging from $15D_0/r_0$ to $300D_0/r_0$ in order to assess the WFNet's applicability. The WFNet has as input an image of four sub-pupils of 32 pixels to estimate 54 Zernike or K-L modes. Finally, the modes predicted by the WFNet and the linear estimation of the PyWFS are compared.

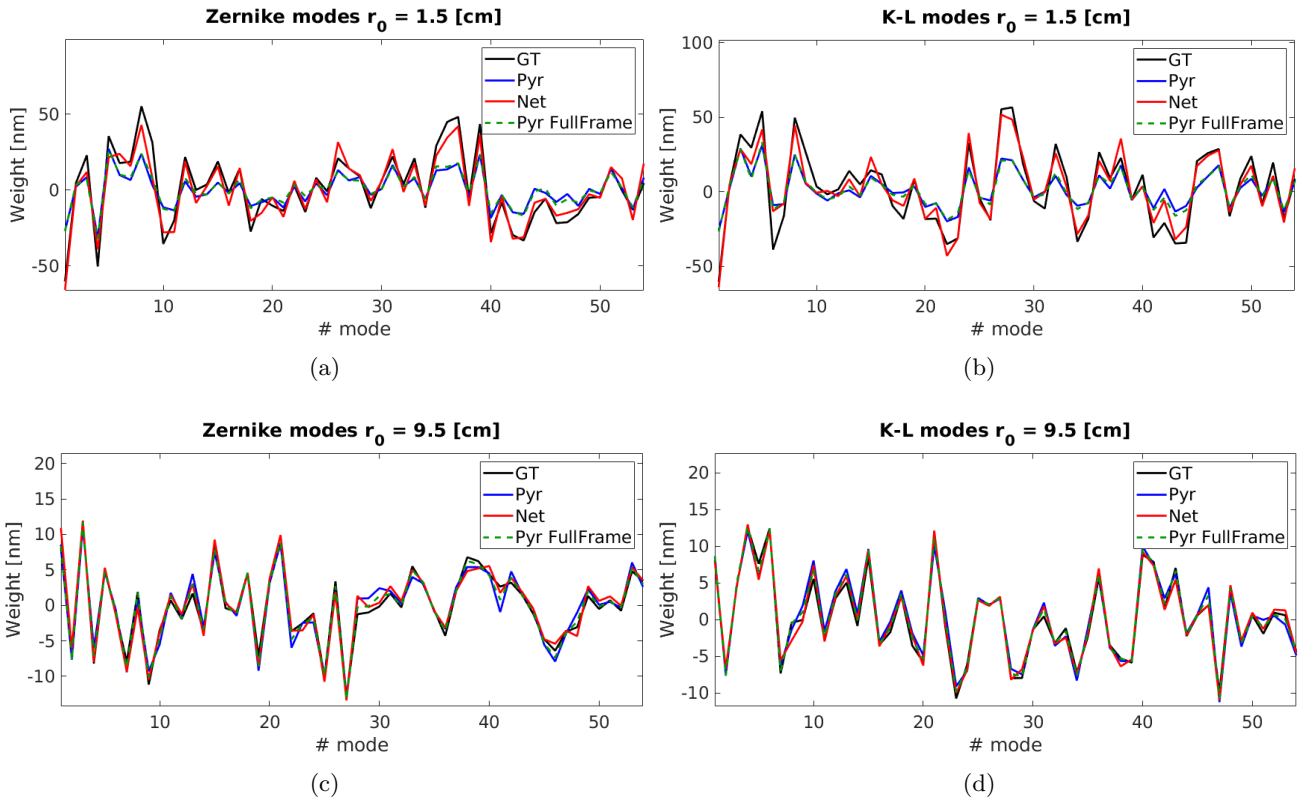

Figure 3: The ground-truth value is given by the black line, the WFNet response is given by the red line and, the blue and green lines represent the classical method for the PyWFS under two different resolutions (32 and 67 pixels per sub-aperture, respectively). (a,b): Comparison for strong-turbulence case: seeing ratio of $100 D_0/r_0$. (c,d): Comparison under weak-turbulence for seeing ratio of 15 D_0/r_0.

3. RESULTS

An example of the WFNet response in a strong turbulence regime $D_0/r_0 \sim 100$ is shown in Fig. 3a) and Fig. 3b). Here, it is possible to observe that the linear response of the PyWFS is significantly lower than the ground-truth value. However, the estimation of the WFNet shows that it can solve linearity issues when the pupil diameter is much larger than r_0. Furthermore, the obtained performance can be compared to a higher modulation case using the linear estimation.

Another example of the WFNet response, now in the case of weak turbulence, where $D_0/r_0 \sim 16$, is shown in Fig. 3c) and Fig. 3d), where the PyWFS linear estimation is within the linearity range, so the prediction almost matches the ground truth value. In this scenario, the pyramid reaches one of its best sensitivity values. Nonetheless, the WFNet also demonstrates that the CNN can accurately estimate the unseen data during training. Thus, once again, the CNN outperforms the traditional method.

The case for very strong turbulence of $r_0 = 0.1$ cm is shown in Fig. 4. The WFNet method underestimates the K-L modes but, at least, it can still predict a similar shape to the ground-truth behavior in the phase map. In contrast, for the PyWFS method, the prediction was practically null for the cases of 32 and 67 pixels per sub-pupil. In this case, the seeing ratio is 1500 D_0/r_0, and the spatial coherence is 0.17 because the telescope's pupil resolution is 268 pixels. As a result, any pixel's relationship to its neighbors will almost be zero in this case.

Fig 5 shows the linearity and residual response of the sensor for randoms K-L modes. In practice, the WFNet is trained using Fourier-phasemaps. Thus, the orthogonality of the system can be tested by activating a single mode. However, this test still outperforms the traditional PyWFS linear estimation method. In the case of pure

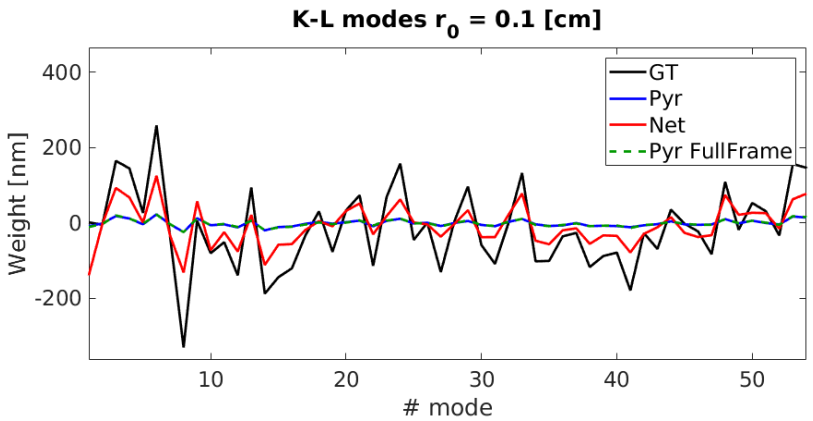

Figure 4: Example for an extremely case of $r_0 = 0.1$ cm. The red line correspond to the WFNet estimation of 54 K-L modes. This behaviour is very similar to the Zernike mode case.

defocus, the PyWFS and the WFNet overestimated close to value 2. Despite this, the WFNet demonstrated more stability under this value, and the estimation is much better in this case.

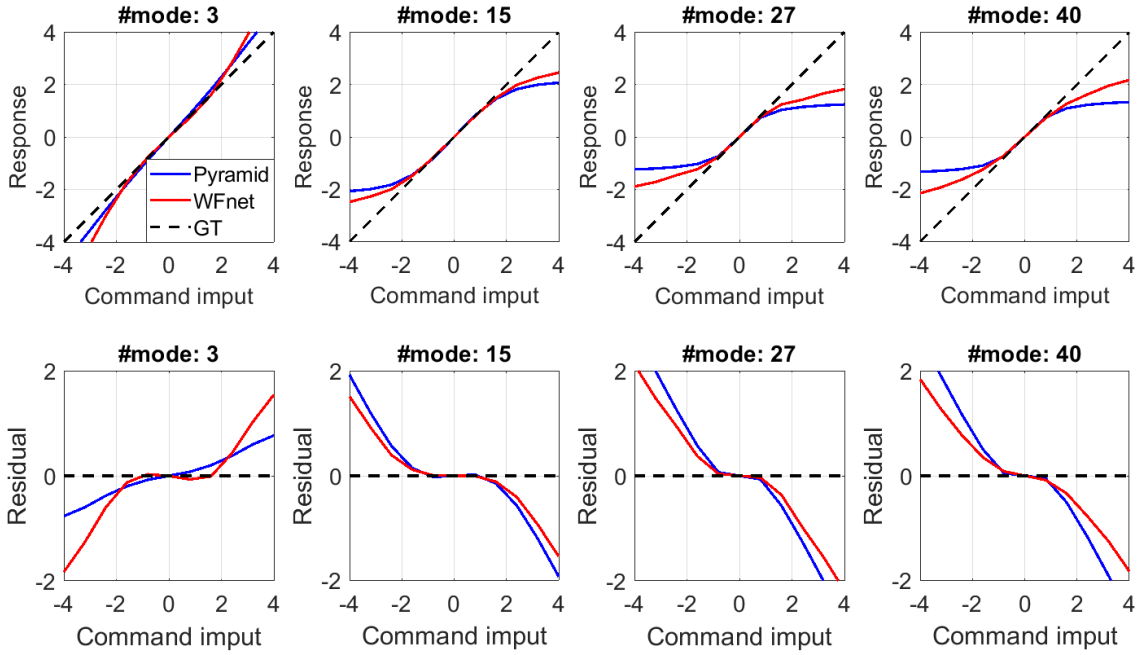

Figure 5: Top: Linearity response for randoms K-L modes. Bottom: Residual behaviour.

The residual analysis, shown in Fig. 6, has been calculated by the RMSE of the difference between the prediction and ground-truth values of the reconstructed phase. Here, high-order modes are not analyzed. In this figure, it is possible to note that the WFNet prediction (red line) has a better response for the Zernike and K-L modes cases (blue line). In both cases, under the same conditions (resolution), the WFNet residual errors are smaller than the PyWFS. For the extremely strength case where $r_0 = 0.1$ cm, the PyWFS show RMSE = 85.11 nm for Zernike modes and RMSE = 81.02 nm for K-L modes, and the WFNet get RMSE = 53.27 nm in Zernike and RMSE = 50.15 nm in K-L modes reconstruction. On the other hand, for good seeing cases where $r_0 = 90$ cm, the PyWFS and WFNet obtained RMSE = 0.57 nm and RMSE = 0.46 nm, respectively. Also, the green line shows the residual error when using 67 pixels of resolution per sub-pupil for the PyWFS. In this case, the

system has the same linearity issues for values smaller than $r_0 = 4$ cm. Despite this, in the good seeing case, the resolution is more important to estimate the modes because the perturbations are under the linearity response range.

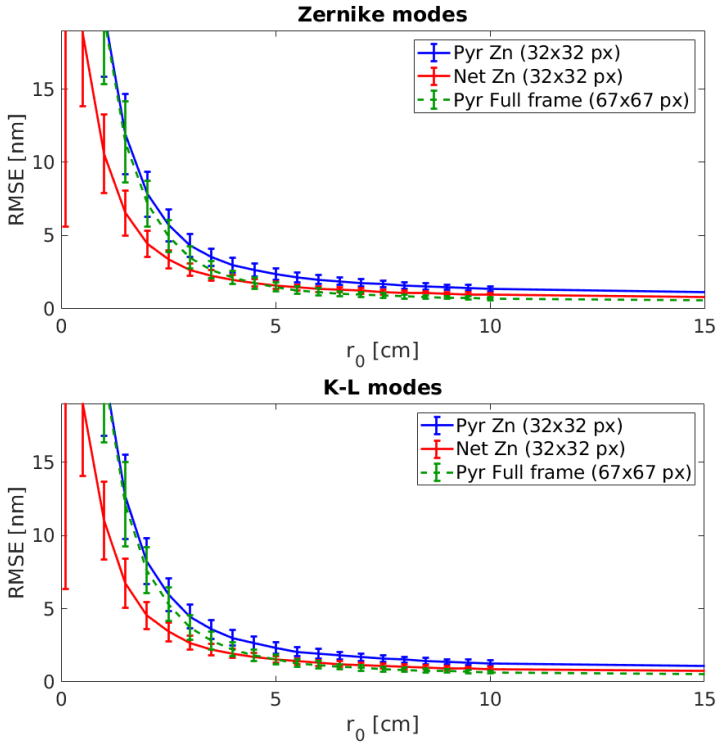

Figure 6: Top: Residual energy using 54 Zernike modes reconstruction. Bottom: Residual energy using 54 K-L modes reconstruction. Blue line: Pyramid reconstruction using sub-pupils of 32 pixels. Red line: WFNet reconstruction using sub-pupils of 32 pixels. Green line: PyWFS using sub-pupils of 67 pixels.

4. CONCLUSIONS

In this work, we evaluated a especially crafted deep convolutional neural network–the WFNet–to provide with estimations of the wavefront aberration modes directly from PyWFS images. Overall, the use of deep neural networks allow to improve the estimation performance as well as the operational range of the PyWFS, especially when considering cases of strong turbulence or bad seeing ratios D_0/r_0.

Under the same conditions, the WFNet outperformed the PyWFS in terms of linearity and reconstruction error. Although this system was not trained to estimate a single mode, its linearity is clearly improved for the specific presented cases. The most important feature of this system is that it can maintain the sensitivity even when the modulation values are decreased.

The residual results of the prediction tests show that the WFNet outperforms the traditional PyWFS method for both strong-turbulence (high seeing ratio) and good seeing. Finally, the results show that the WFNet improves the performance of the PyWFS in the linear regime, and the results in Fig. 4 show promising results for the use of machine-learning architectures in highly sensitivity applications requiring adaptive optics.

ACKNOWLEDGMENTS

ANID-ALMA (ASTRO20-0088), ECOS-ANID (C20E02), STIC-AMSUD (21-STIC-09), FONDECYT (1221883) and ANID / Scholarship Program / DOCTORADO BECAS CHILE/2022 - 21221399

REFERENCES

[1] Ragazzoni, R., "Pupil plane wavefront sensing with an oscillating prism," *Journal of modern optics* **43**(2), 289–293 (1996).

[2] Wang, S., Wei, K., and Zheng, W., "Modulation-nonmodulation pyramid wavefront sensor with direct gradient reconstruction algorithm on the closed-loop adaptive optics system," *Opt. Express* **26**, 20952–20964 (Aug 2018).

[3] Lee, J.-H., Doel, A., and Walker, D., "Pupil plane wavefront sensing with a static pyramidal prism: Simulation and preliminary evaluation," *J. Opt. Soc. Korea* **4**, 1–6 (Mar 2000).

[4] Burvall, A., Daly, E., Chamot, S. R., and Dainty, C., "Linearity of the pyramid wavefront sensor," *Optics express* **14**(25), 11925–11934 (2006).

[5] Fauvarque, O., Neichel, B., Fusco, T., Sauvage, J.-F., and Girault, O., "General formalism for fourier-based wave front sensing: application to the pyramid wave front sensors," *Journal of Astronomical Telescopes, Instruments, and Systems* **3**(1), 019001 (2017).

[6] Chambouleyron, V., Fauvarque, O., Janin-Potiron, P., Correia, C., Sauvage, J.-F., Schwartz, N., Neichel, B., and Fusco, T., "Pyramid wavefront sensor optical gains compensation using a convolutional model," *Astronomy &amp Astrophysics* **644**, A6 (nov 2020).

[7] Vera, E., Guzmán, F., and Weinberger, C., "Boosting the deep learning wavefront sensor for real-time applications," *Applied Optics* **60**(10), B119–B124 (2021).

[8] Nishizaki, Y., Valdivia, M., Horisaki, R., Kitaguchi, K., Saito, M., Tanida, J., and Vera, E., "Deep learning wavefront sensing," *Optics express* **27**(1), 240–251 (2019).

[9] Conan, R. and Correia, C., "Object-oriented matlab adaptive optics toolbox," in [*Adaptive optics systems IV*], **9148**, 91486C, International Society for Optics and Photonics (2014).

[10] Vérinaud, C., "On the nature of the measurements provided by a pyramid wave-front sensor," *Optics Communications* **233**(1-3), 27–38 (2004).